Length-dependent Intramolecular Coil-to-Globule Transition in Poly(ADP-ribose) Induced by Cations

Tong Wang*[1], Kush Coshic*[2], Mohsen Badiee*[3], Aleksei Aksimentiev[2#], Lois Pollack[1#], Anthony K. L. Leung[3,4#]

[1]School of Applied and Engineering Physics, Cornell University, Ithaca, NY 14853, USA
[2]Department of Physics, University of Illinois Urbana Champaign, Urbana, IL 61801, USA
[3]Department of Biochemistry and Molecular Biology, Bloomberg School of Public Health, Johns Hopkins University, Baltimore, MD 21205, USA
[4]Department of Molecular Biology and Genetics, Department of Oncology, Department of Genetic Medicine, School of Medicine, Johns Hopkins University, Baltimore, MD 21205, USA

*co-first authors; [#]co-corresponding authors

Correspondence:
Anthony K. L. Leung (anthony.leung@jhu.edu)
Lois Pollack (lp26@cornell.edu)
Aleksei Aksimentiev (aksiment@illinois.edu)

ABSTRACT

Poly(ADP-ribose) (PAR), as part of a post-translational modification, serves as a flexible scaffold for noncovalent protein binding. Such binding is influenced by PAR chain length through a mechanism yet to be elucidated. Structural insights have been elusive, partly due to the difficulties associated with synthesizing PAR chains of defined lengths. Here, we employ an integrated approach combining molecular dynamics (MD) simulations with small-angle X-ray scattering (SAXS) experiments, enabling us to identify highly heterogeneous ensembles of PAR conformers at two different, physiologically relevant lengths: PAR_{15} and PAR_{22}. Our findings reveal that numerous factors including backbone conformation, base stacking, and chain length contribute to determining the structural ensembles. We also observe length-dependent compaction of PAR upon the addition of small amounts of Mg^{2+} ions, with the 22-mer exhibiting ADP-ribose bundles formed through local intramolecular coil-to-globule transitions. This study illuminates how such bundling could be instrumental in deciphering the length-dependent action of PAR.

GRAPHICAL ABSTRACT

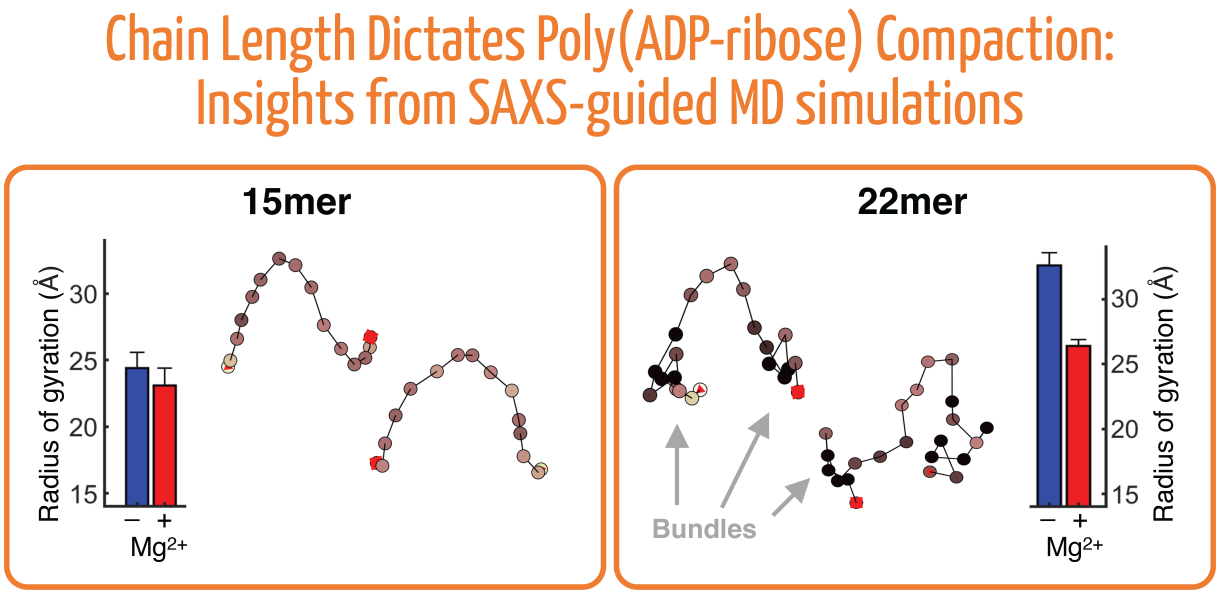

INTRODUCTION

Poly(ADP-ribose) (PAR) is a nucleic acid-like polymer produced in cells as a post-translational modification by ADP-ribosyltransferases commonly known as PARPs (Fig. 1A).[1,2] PAR is composed of the same phosphate and nucleoside building blocks as RNA. However, because it contains only adenines, PAR is unlikely to form intramolecular base pairs and is thus likely to be disordered.[3] Functionally, PAR may serve as a signal mediator, conjugating to proteins in restoring homeostasis after stress, such as DNA damage and inflammation (Fig. 1B).[4-8] PAR may also serve as a scaffold for protein complex or biomolecular condensate formation, where its negative charge allows for multivalent noncovalent interactions with basic proteins.[9,10]

In mammalian cells under extreme stress or high doses of DNA-damaging agents, homopolymers with around 200 ADP-ribose units have been observed.[11] However, under normal and mildly stressed conditions, PAR oligomers exhibit a size distribution that ranges from as few as 2 units to approximately 20 units.[12-14] PAR can bind positively charged ligands potentially through a combination of electrostatic interactions and conformational fit, as shown for other nucleic acids. PAR interacts with its binding partners through reader motifs, such as the PAR binding motif, PAR binding zinc finger, and the RNA-binding RGG and RRM moieties.[15] The binding affinity of PAR to proteins depends on their chain length on a global scale, where its specificity could be even down to a single ADP-ribose difference (Fig. 1C, D).[16–20] In certain cases, such as with oncoprotein DEK, a threshold PAR length is necessary for appreciable binding to occur.[21] Moreover, 4-mer PAR does not induce the condensation of FUS (a key protein associated with multiple neurodegenerative diseases), whereas 8- and 16-mer do, and 32-mer drives its aggregation (Fig. 1E).[22] So, how does a simple homopolymer achieve such length-specific protein interactions? We posited that PAR may adopt distinct structures based on its polymer length.

Despite its functional importance, PAR's 3D structure has not been much investigated, partly due to difficulties associated with synthesizing PAR chains of defined lengths. Adding to this complexity is the experimental difficulty of probing disordered macromolecules using traditional structural biology techniques like X-ray crystallography and electron microscopy, which require sample fixation. Further challenges arise in interpreting the dynamic structural ensembles that such molecules adopt, raising the need for additional analysis and visualization methods. Although PAR's functionality is influenced by its polymer length, it is uncertain whether a single structural

model can capture the length-dependent richness of biological PAR activity. A detailed examination of the structural features of different lengths of PAR could elucidate its length-dependent conformations and potentially clarify its selective interactions with binding partners.

Here, we coupled molecular dynamics (MD) simulations and small-angle X-ray scattering (SAXS) measurements to determine structural ensembles of PAR in solutions in a range of ionic conditions. Our MD simulations showed PAR_{22} undergoes steady compaction as cation concentration increases, with Mg^{2+} inducing greater compaction compared to Na^{+}, corroborating recent findings.[23] Next, we selected conditions close to physiological ionic strength and applied MD-SAXS to extract structural ensembles for two different PAR lengths, PAR_{15} and PAR_{22}. These lengths are not only commonly observed in mammalian cells but are also within the bacterial PARP-produced range.[12-14,24,25] We defined structural order parameters to categorize backbone conformations across the structural ensembles. Our results indicate that both backbone tortuosity and base stacking contribute to PAR compaction in unique ways for both lengths. Additionally, we compared PAR to RNA and identified specific structural features that may contribute to their distinct biological roles. Lastly, by decomposing the structural ensembles into easily visualizable components using 3D class averaging in real space, we identified bundles of ADP-ribose units in PAR_{22}, but not PAR_{15}, in the presence of Mg^{2+}. We postulated that these bundles create localized regions of high negative charges. This detailed structural description offers a possible explanation for differences in the conformations and binding behaviors exhibited by PARs of different lengths.

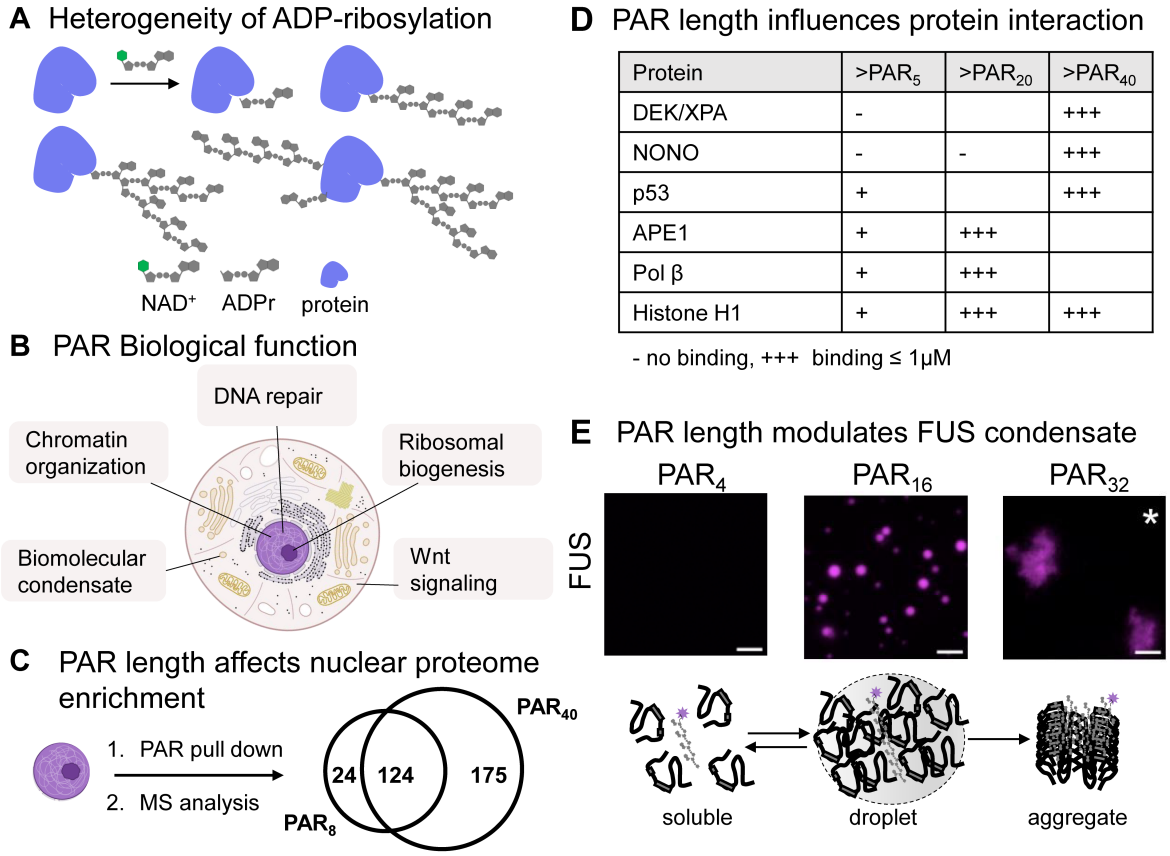

Protein	>PAR_5	>PAR_{20}	>PAR_{40}
DEK/XPA	-		+++
NONO	-	-	+++
p53	+		+++
APE1	+	+++	
Pol β	+	+++	
Histone H1	+	+++	+++

- no binding, +++ binding ≤ 1μM

Figure 1. **Biological functions of PAR and its relationship to chain length.** (A) ADP-ribosylation is heterogenous, presented as monomeric, linear or branched polymer forms as poly(ADP-ribose) or PAR. (B) PAR mediates various cellular processes at distinct subcellular locations. (C) Pulldown of PAR-binding proteins in nuclear lysate coupled with mass spectrometry analysis indicates a preference of proteome to the length of PAR (data reproduced from Dasovich et al with permission).[18] (D) Biochemical studies showing that the strength of PAR-proteins interaction is influenced by the chain length. (E) PAR modulates the formation and dynamics of biomolecular condensates linked to human disease. In vitro microscopic studies showing that PAR chain length influences material properties of FUS condensates, both at 1 μM; scale bar, 5 μm. These images were adopted from Rhine et al. with permission.[22]

EXPERIMENTAL SECTION

Molecular dynamics (MD) simulations

All MD simulations were performed using NAMD2.14,[26] the CHARMM36 parameter set for protein and DNA,[27] TIP3P water model,[28] and a custom hexahydrate model for magnesium ions along with the CUFIX corrections to ion–nucleic acid interactions.[29] Multiple time stepping was used: local interactions were computed every 2 fs, whereas long-range interactions were computed every 6 fs.[30] All short-range nonbonded interactions were cut off starting at 1 nm and completely cut off by 1.2 nm. Long- range electrostatic interactions were evaluated using the particle-mesh Ewald method computed over a 0.11 nm spaced grid.[31] SETTLE and RATTLE82 algorithms were applied to constrain covalent bonds to hydrogen in water and in non-water molecules, respectively.[32,33] The temperature was maintained at 300 K using a Langevin thermostat with a damping constant of 0.5 ps^{-1}, unless specified otherwise. Constant pressure simulations employed a Nose-Hoover Langevin piston with a period and decay of 200 and 50 fs, respectively.[34] Energy minimization was carried out using the conjugate gradients method. Atomic coordinates were recorded every 9.6 picoseconds, unless specified otherwise. An example MD timeseries plot is shown in Figure 2B. Visualization and analysis were performed using VMD and MDanalysis.[35–37]

CHARMM-compatible force field parameters for PAR were obtained by combing existing parameters for chemically similar moieties. Specifically, a custom patch was written to define a PAR residue (PAR), whereby the oxygen atom on the terminal phosphate group of an ADP molecule (atom O5D) was connected to the ribose sugar (atom C5D) using analogy from NADP. Similarly, a custom patch (BND) connected the ribose (atom O1D) with ADP (C2′). With these two patches, a PAR molecule of arbitrary number of monomers could be defined. Separate patches were defined for the terminal atoms, a hydrogen on the O1D atom of the ribose (1TER) and an OH group on the C2′ atom of ADP (2TER). The topology and parameter files for a PAR residue are provided in Supplementary Materials.

Small-angle X-ray scattering (SAXS)

Solution SAXS experiments on PAR_{15} and PAR_{22} were performed at the ID7A1 BioSAXS beamline at the Cornell High Energy Synchrotron Source and the 16-ID Life Science X-ray

Scattering beamline at the National Synchrotron Light Source II of Brookhaven National Laboratory.[38,39] Radial integration and data reduction was performed in BioXTAS RAW to obtain 1D scattering profiles, plotting scattering intensities (I, in arbitrary units) as a function of momentum transfer (q, in $Å^{-1}$).[40] PAR was assayed at 60μM, 40μM, and 20μM concentrations to observe for interparticle effects at low q, and these were corrected when present by linearly extrapolating each point at $q < 0.05$ $Å^{-1}$ to the zero-concentration limit. Radii of gyration were obtained through Guinier analysis,[41] approximating the scattering profile at $(q\ R_g) < 1.3$ as a Gaussian function:

$$I(q) = I(0)e^{-\frac{q^2 {R_g}^2}{3}}$$

Guinier analyses are shown in Fig. S1. Data were plotted in the size-normalized Kratky format to emphasize changes in overall macromolecular shape. The molecular form factor (MFF) model was fit to the scattering data and used to describe the arrangement of the PAR chain ensembles relative to the theta state through the Flory (v) parameter (Fig. S2).[42,43] Scattering data are deposited on the Small Angle Scattering Biological Data Bank (SASBDB) with the identifiers SASDSJ5, SASDSK5, SASDSL5, SASDSM5.

Determining PAR structural ensembles

To provide a diverse pool of structures for PAR, we sampled the MD trajectories in 1 nanosecond snapshots, obtaining a set of 1000-1200 individual structures over a broad, continuous conformational range. Fig. S3 shows the structural ensembles parameterized in Cartesian space by their R_g and R_{EE}. CRYSOL v2.0 was used to compute the theoretical scattering profile of all structures in the SAXS regime, with a maximum order of harmonics of 15, Fibonacci grid order of 18, 0.3 $Å^{-1}$ maximum scattering angle, and 61 calculated data points.[44]

The raw MD simulations were seen to approximate well the overall size of the conformational ensembles but not their overall shape. This is evidenced by the discrepancies between the summed theoretical scattering of all structures in the pool and the experimental scattering beyond the low q regime ($q > 0.03$ $Å^{-1}$) (Fig. S4). To provide an accurate depiction of the solution-state ensemble of structures that the molecules sample, the information content of the SAXS data was leveraged

through EOM v2.1 (ATSAS, EMBL Hamburg, Germany).[45,46] Briefly, subsets of the pool of structures were sampled and the summated theoretical SAXS profile of the subset of structures was computed and fit to the experimental SAXS profile – the process was iterated until agreement with the experimental data is reached. EOM was run over 1000 generations with 50 ensembles, 20 curves and 10 mutations per ensemble, over 100 iterations. This was found to yield convergence of the fit to the experimental SAXS data, with χ^2 values of 0.1 – 0.4 and the SAXS profiles of the final pool post-EOM falling within error of the experimental measurement across the entire q range (Fig. S4). Introducing more iterations into the algorithm beyond that executed was not found to improve convergence of the χ^2 meaningfully, except for PAR_{22} in 100 mM NaCl where 10000 iterations were employed. The final ensembles were assessed to fall along a continuous distribution in their R_g, R_{EE}, and maximal dimensions, with no implausible bimodalities.

RESULTS

PAR Compaction and Structural Dynamics Influenced by Cationic Environment

To build a comprehensive understanding of PAR's conformational behavior in different environments, we performed a series of MD simulations on PAR_{22}. A typical simulation began with the PAR polymer in a fully extended state, submerged in a large volume of electrolyte solution (Fig. 2A). Within the first 50 ns of equilibration, the polymer transitioned to a more compact state (Fig. 2B). All conformations were characterized using the end-to-end distance (R_{EE}) and the radius of gyration (R_g) of the polymer.

Prior research, including circular dichroism analyses of mixed-chain length PAR molecules and our recent single molecule Förster resonance energy transfer (smFRET) measurements, revealed that PAR compaction is sensitive to cations.[23,47] These findings align with established knowledge that nucleic acid structures are sensitive to their cationic environment.[48,49] In our MD simulations, we observed that both R_{EE} and R_g steadily decrease as the concentration of Na^+ increases (Fig. 2C). Visualization of typical conformations indicates a transition: PAR adopts an extended, linear-like conformation at low salt concentrations and changes to a more compact, globular conformation at high salt concentrations (Fig. 2D). In the compact state, Na^+ ions screened the backbone charge of PAR_{22}, facilitating proximity between ADP-ribose units (Fig. 2D).

162 We extended our simulations to examine the impact of Mg^{2+} on PAR conformation and found an
163 extreme sensitivity to this cation (Fig. 2E). In this set of simulations, we kept the total charge of
164 cations equal in magnitude to the charge of PAR_{22}, while varying the fraction of the charge
165 neutralized by Mg^{2+} from 0 to 100% (Fig. 2E, red points). Remarkably, increasing the fraction of
166 charge neutralization by Mg^{2+} from 25 to 50% led to a two-fold reduction in R_{EE}. Further analysis
167 revealed that Mg^{2+} ions do not compact PAR in a homogenous manner; instead, they induce the
168 formation of highly compacted globules separated by extended polymer chains (Fig. 2F, S1). This
169 compaction was visualized over time across different systems using heatmaps that depict the
170 number of neighboring ADP-ribose units within a 10 Å radius of each PAR residue (Fig. S5).
171 Counting the net charge within this radius over time further revealed the interplay between spatial
172 localization and charge (Fig. S6). Interestingly, the globular conformations observed at a
173 neutralizing concentration of Mg^{2+} (100%, 7 mM) closely resemble those at much higher $MgCl_2$
174 concentrations (50 mM). These data indicate that PAR_{22} is optimized for compaction even at Mg^{2+}
175 concentrations much closer to physiological levels. This high sensitivity of PAR to Mg^{2+}, including
176 the formation of locally compacted domains (Movie S1 and S2), suggests that Mg^{2+} may play a
177 structural role. Beyond simply screening electrostatic charges, Mg^{2+} may trigger a transition of
178 PAR from an elongated polymer to a condensed globule.

179 To further quantify the effect of adding Mg^{2+}, we conducted simulations with a fixed NaCl
180 concentration of 50 mM while varying the $MgCl_2$ concentration (Fig. 2G). These conditions align
181 with those previously examined through smFRET experiments.[23] Our simulation showed that, in
182 the presence of Mg^{2+}, PAR transitioned from extended to compacted states and exhibited
183 conformations where both states coexist within the same molecule (Fig. 2H, S1, S2). When
184 compared to simulations in pure NaCl solvent (Fig. 2C-D), the onset of compact conformations
185 occurred at significantly lower $MgCl_2$ concentrations. Specifically, a complete globular collapse
186 occurred at 21 mM of $MgCl_2$, in contrast to 2 M NaCl. Furthermore, over 39% of total compaction
187 was achieved at a $MgCl_2$ concentration as low as 3 mM. These observations are consistent with
188 previous studies on single-stranded RNA, where only 5 mM $MgCl_2$ was required to induce the
189 same R_g change as 600 mM NaCl.[48]

190 Taken together, our MD simulations show that PAR is structurally dynamic, adopting a range of
191 conformations depending on the ionic environment. In the absence of Mg^{2+}, PAR adopts extended

conformations at physiological Na^+ concentrations. However, even small amounts of Mg^{2+} can trigger local compaction of the PAR polymer—a structural transition that we further explored in the remainder of this study.

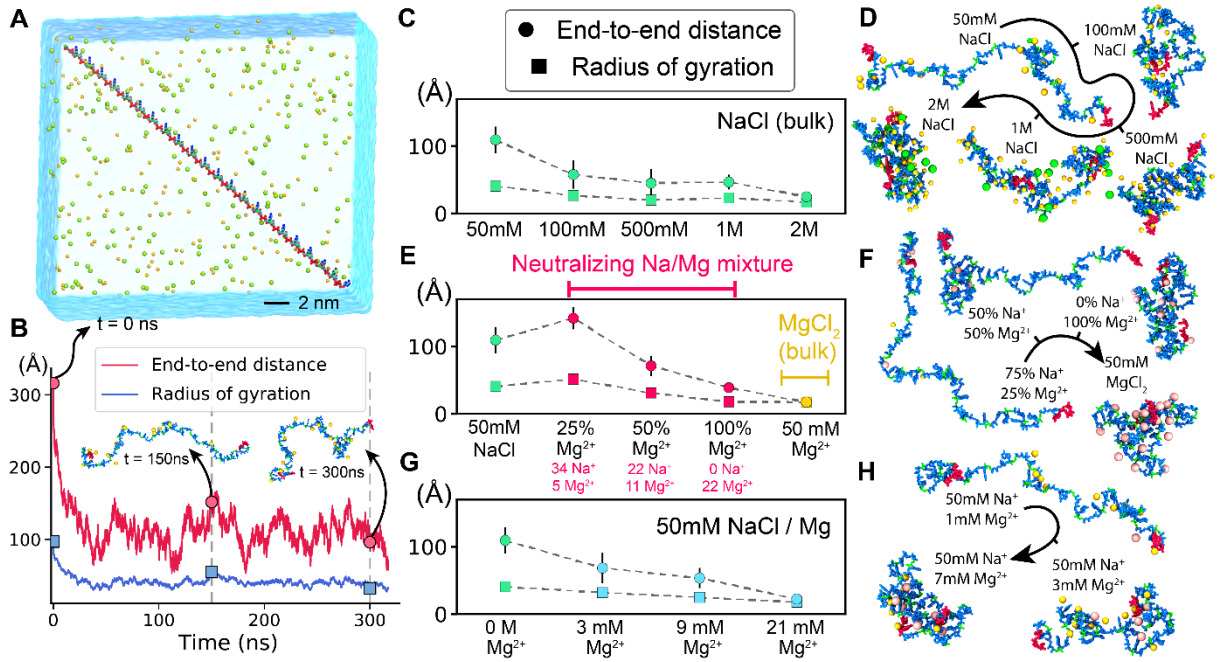

Figure 2. Molecular dynamics simulations of a 22-mer PAR polymer. (A) Initial configuration of a typical simulation system. One 22-mer PAR polymer is placed in electrolyte solution (semitransparent molecular surface) containing 50 mM of NaCl. (B) End-to-end distance (R_{EE}) and radius of gyration (R_g) of a PAR molecule as a function of time simulated in 50 mM NaCl electrolyte. (C,E,G) Average equilibrium end-to-end distance (circles) and radius of gyration (squares) of the 22-unit PAR polymer at various ion conditions. Dashed lines connect the points to guide the eye. Each data point represents a 250-ns trajectory average, after exclusion of the first 50 ns in each simulation where the molecule started in an extended state. (D,F,H) Representative snapshots of PAR conformation at the end of a 300 ns equilibration performed at the specified ion concentration conditions. The O3′, C3′, C4′, C5′, and O5′ atoms of PAR are shown in green whereas all other atoms in blue. Na^+ (yellow), Cl^- (green) and Mg^{2+} (pink) ions located within 6 Å of PAR are shown as spheres. The ends of the PAR chains are depicted in red.

SAXS Reveals Distinct Compaction for PAR_{15} and PAR_{22} with Mg^{2+}

Having surveyed a broad range of ionic conditions in the MD simulations of PAR, we focused on specific conditions for experimentally identifying various structural parameters of PAR using

SAXS. We examined PAR_{15} and PAR_{22}, both of which are found in normal and cancer cells, with the shorter one being more abundant.[12-14] The SAXS experiments were conducted in a 100 mM NaCl environment to approach physiological conditions, and we assessed the impact of adding 1 mM $MgCl_2$ on PAR compaction.

SAXS provides us with the overall size of the PAR structural ensembles, represented by the R_g values (Fig. 3A-B).[41] In a 100 mM NaCl solution, PAR_{15} had an R_g of 24.4 ± 1.2 Å, while PAR_{22} had an R_g of 32.6 ± 0.5 Å (Fig. 3B). Adding 1 mM Mg^{2+} led to a 5.3% reduction in R_g for PAR_{15} and a significant 19.0% reduction for PAR22, indicating a greater compacting effect on the longer PAR_{22} molecule.

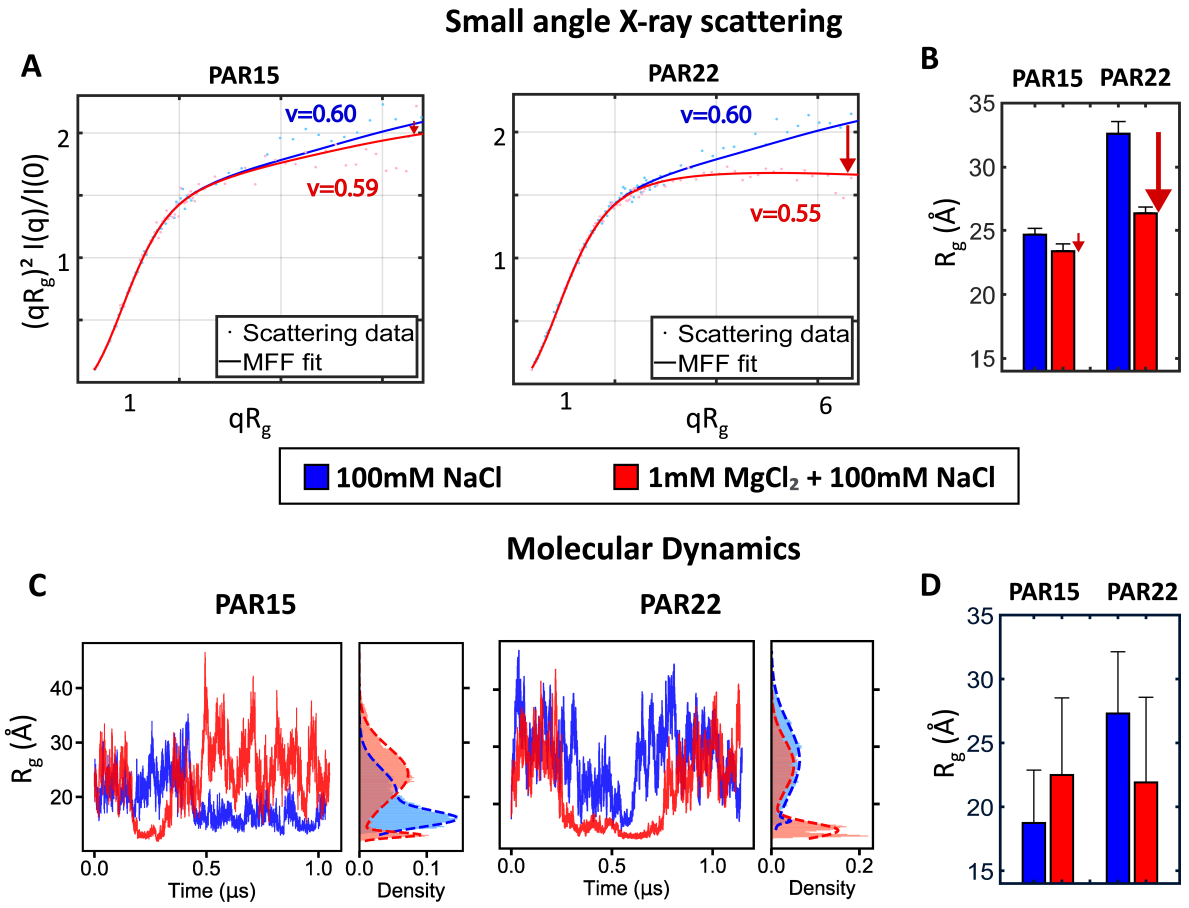

Figure 3. **Length-dependent collapse of PAR polymer.** (A) SAXS profiles of PAR_{15} and PAR_{22} in 100 mM NaCl with (red) and without (blue) the addition of 1 mM $MgCl_2$. Data are plotted in dimensionless Kratky axes, normalizing out size differences and emphasizing changes in shape and disorder in the mid-angle scattering regime. Experimental scattering is shown in light colored points and solid lines show molecular form factor (MFF) model fits to the data,

extracting the Flory scaling parameter ν (Fig. S2).[42] Reduced χ^2 values for the fits are: 0.129 & 0.168 for PAR_{15} and 0.421 & 0.369 for PAR_{22}, without and with $MgCl_2$ respectively. (B) SAXS-derived R_g values for PAR_{15} and PAR_{22} in the conditions assayed. Error bars show errors in the linear Guinier fits used to extract R_g. (Fig. S1) (C) Radius of gyration of PAR_{15} and PAR_{22} polymers in MD simulations carried out at 100 mM NaCl, with and without 1 mM $MgCl_2$. The histograms next to the timeseries plots illustrate the distribution of the R_g values. (D) Average simulated radius of gyration of PAR_{15} and PAR_{22} determined as a weighted mean of the two-Gaussian fit to the histograms.

We also calculated the Flory (ν) parameters for both PAR lengths at each salt concentration to understand their interaction with its surrounding solvent (Fig. 3A, S4).[42] Kratky plots were used for clearer data visualization, emphasizing the mid-angle scattering regime where the overall shape and degree of disorder of the molecular ensemble can be discerned.[50]

When Mg^{2+} was absent, fits to SAXS profiles for both PAR_{15} and PAR_{22} yielded a ν value of 0.60 ± 0.02 and 0.60 ± 0.01, respectively. This ν value is expected for a self-avoiding random walk, suggesting that similar polymer properties for both PAR lengths in a 100 mM Na^+ environment. The ratio of R_g values between PAR_{22} and PAR_{15} (32.6 Å / 24.4 Å = 1.34) is consistent with the expected behavior for molecules with ν = 0.6, according to the classical scaling law, $R_g \alpha \text{length}^{\nu}$. This agreement provides additional confidence in this polymer description of PAR.

When Mg^{2+} was introduced, both PAR lengths underwent a decrease in ν, more pronounced for PAR_{22} (ν = 0.55 ± 0.01) than for PAR_{15} (ν = 0.59 ± 0.02). These changes point to a stronger progression of PAR_{22} toward a theta state, where no interactions are present between polymer and solvent (Fig. 3A, S4).[51] Overall, these experimental results indicate that the longer PAR_{22} undergoes more significant conformational change when exposed to Mg^{2+} compared to its shorter counterpart, PAR_{15} (Fig. 3B).

MD-SAXS Reveals Mg^{2+} Increases Tortuosity and Base Stacking in PAR_{22} Than PAR_{15}

To examine specific conformations in PAR responsible for the observed differences in size and shape, we integrated SAXS data with additional MD simulations. We extended the simulations to 1 μs to capture a broader range of conformations for both PAR lengths. During these simulations,

we noticed that the PAR conformations oscillated between extended and compact conformations (Fig. 3C). Because of this bimodal behavior, and since the duration of simulation duration was comparable to the lifetime of each state, we were unable to determine average R_g values for direct comparison (*i.e.*, a large error margin when averaging R_g values across the entire simulations; Fig. 3D). Instead, we employed an ensemble optimization method (EOM) to refine the full pool of MD structures using SAXS data.[45,46] The computed scattering profiles from the refined ensembles closely matched the experimentally measured SAXS profiles in molecular shapes and overall R_g values (Fig. 4A-B, S5-7).

Next, we analyzed how PAR conformation and compaction change with Mg^{2+} for both PAR_{15} and PAR_{22} (Fig. 4C). The refined pools displayed a relatively uniform distribution of structures around an average, with no pronounced bimodality, as one would expect for a macromolecular ensemble (Fig. S3). Importantly, the final fits between the EOM structural ensembles and SAXS data consistently fell within the experimental error margin, with ensemble R_g values in agreement across both methods (Fig. S4).

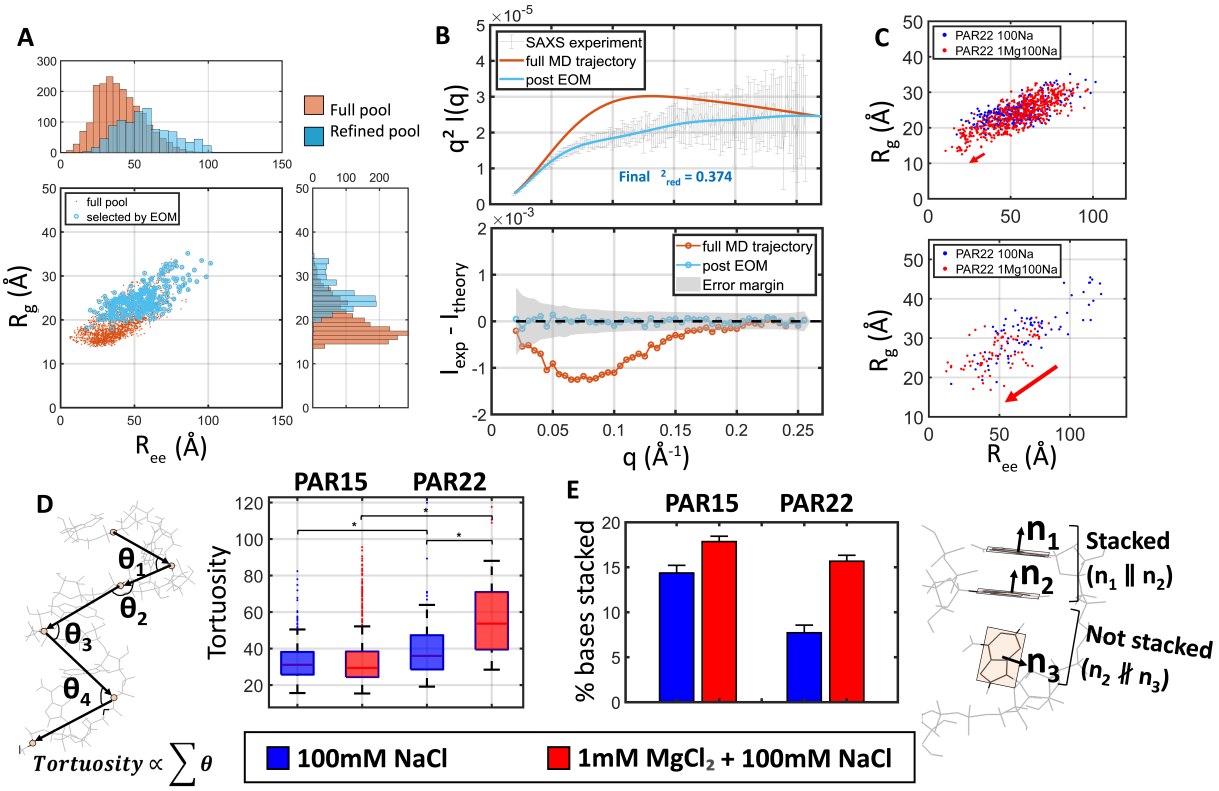

Figure 4. Determining structural ensembles for PAR using MD and SAXS. As an example, the case for PAR_{15} in 100 mM NaCl is shown. The same plots for PAR_{22} are shown in Fig. S3-

4. (A) The pool of structures from the entire MD simulation is shown in orange, and the subset ensemble that agrees with the SAXS data in blue. Structures are parameterized in $\{R_g,R_{EE}\}$ space. 1D histograms are weighted by the prevalence of each structure in the final ensembles. (B) Final agreement of the structural ensemble determined by EOM to the SAXS data, compared to initial agreement of the structural ensemble of all MD conformers. Residuals are shown in the bottom plot. (C) Ensembles of EOM-determined PAR structures, with and without Mg^{2+} for PAR_{15} and PAR_{22}. Arrows show differential shifts to more compact states with the addition of Mg^{2+}. D) Tortuosities and E) Fraction of adenine bases that are stacked in each structural ensemble of PAR. For the tortuosity plot, '*' denotes $p<0.05$. For the base stacking plot, error bars show standard error.

With refined ensembles now available for all conditions (PAR_{15} and PAR_{22}, both with and without Mg^{2+}), we analyzed the included structures. We computed the tortuosity index of each structure in the identified ensemble to gauge their backbone conformations (Fig. 4D). Tortuosity quantifies how "twisted" the polymer is compared to a straight line drawn connecting its endpoints. Without Mg^{2+}, PAR_{22} has a significantly greater mean tortuosity across its structural ensemble than PAR_{15}, indicating a more twisted backbone (Fig. 4D), despite the identical ν values. Interestingly, introducing Mg^{2+} significantly increased the tortuosity of PAR_{22}, but not PAR_{15} (Fig. 4D).

We also examined the role of π-π stacking in driving PAR chain compaction (Fig. 4E). Such interactions are particularly common among adenine bases and are known to induce intra-chain helicity in adenine-rich RNA sequences.[48] In the presence of 1 mM $MgCl_2$, PAR_{15} underwent a 24% increase in base stacking events, whereas PAR_{22} exhibited a 103% increase (Fig. 4E). This greater frequency of π-π interactions between adenine bases could contribute to the greater compaction of PAR_{22} compared to PAR_{15}.

PAR_{22} Displays ADP-ribose Bundles

To further analyze the structural ensembles revealed by EOM, we parameterized the structures according to their $\{R_g,R_{EE}\}$ values and performed hierarchical clustering.[52] Using this approach, we found that the ensembles are highly heterogeneous: R_g and R_{EE} values covered 30 Å and 100 Å ranges, respectively. Through hierarchical clustering, we grouped structures into clusters with similar size, ranging from highly extended to highly compact (Fig. S7).

To elucidate unique conformational features within these clusters, we computed heatmaps of pairwise distances between bases in EOM-selected structure ensembles (Fig. S8). These heatmaps revealed how ADP-ribose bases are connected along the PAR chains. In these maps, off-diagonal regions with shorter distance implies the crowding of distal bases. For $PAR_{15,}$ the heatmap revealed proximity mainly along the diagonal of the heatmap. This trend progressed monotonically towards the corners, suggesting that the molecule predominantly adopts relatively featureless extended conformations, irrespective of the presence or absence of $MgCl_2$ (Fig. S8A). In contrast, PAR_{22}'s heatmap showed significant connections, or close contacts, between bases that are close together (blue regions, slightly off-diagonal). One such region appeared in the 100 mM NaCl map (upper left corner), while two were evident when 1 mM $MgCl_2$ was added (upper left and lower right corners, Fig. S8B). These off-diagonal regions indicate a local bundle of non-adjacent bases at the end(s) of the molecule, corroborating findings of local compaction initially identified in our MD simulations (Fig. 2).

We next considered the role of π- π stacking in these distinct ensembles. For PAR_{15}, regions of proximity (*i.e.*, low inter-base distance) correlated somewhat with where base stacking occurs, mainly along the diagonals (Fig. S8A). Yet, for PAR_{22}, these off-diagonal low-distance regions were not enriched with base stacks (Fig. S8B). Most stacking events occurred between adjacent bases along the chain. Thus, while PAR_{22} has more base stacking with 1 mM Mg^{2+} than PAR_{15} in general (Fig. 4E), the observed ADP-ribose bundles appear unrelated to base stacking. Rather, local chain compaction due to the proximity of the PAR phosphate backbone to an Mg^{2+} ion likely triggers the intra-chain coil-to-globule transitions that lead to these bundles. This transition is evident in individual frames of the MD simulations, where the compaction correlates to some extent with proximity of Mg ions to the backbone (Fig. S9, Movie S2). Taken together, our analyses on the heterogeneous structural ensembles confirm the presence of ADP-ribose bundle formation unique to PAR_{22}.

Distinct Backbone Conformations for PAR_{15} and PAR_{22}

Hierarchical clustering partitioned the structural ensembles into groups based on the overall size of each structure; however, deriving a more concise description of the PAR backbone conformations was challenging due to a variety of poorly related structures populating in any size

subgroup (Fig. S7). Inspired by 2D classification of structures in single particle cryo-electron microscopy and graph theory,[53] we grouped the ensembles into unique, interrelated conformational subclasses. By applying 3D spatial alignment into network graphs and performing spectral clustering, we captured all conformations present in the ensembles, with no graph outliers (Fig. S10). The low spatial variation between the constituent structures of these subclasses (Fig. 5 and S11) supports that our algorithm effectively identified sensible classes, justifying the subsequent averaging to depict a single representative conformation in each class.

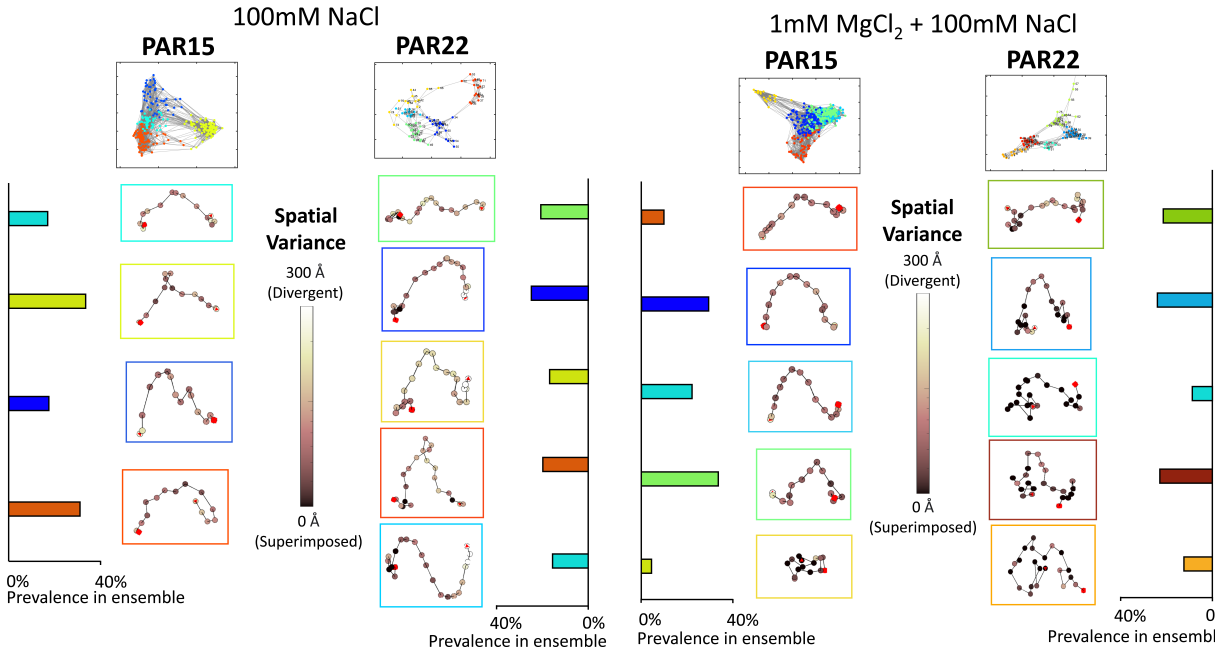

Figure 5. Backbone structural features of PAR_{15} vs PAR_{22} identified through spectral clustering. PAR_{15} and PAR_{22} in 100 mM NaCl, both without and with the presence of 1 mM $MgCl_2$ is shown (A-D). Top plots show the graphs of PAR structures in each ensemble, color coded by the clusters identified by K-means. The box colors around each identified subclass matches their locations in the graphs. Wireframe models show the mean PAR backbone conformation in each case – each dot represents the mean position of each pair of phosphorus atoms across the entire subclass, colored by the degree of spatial variance present across that class. Red squares denote the 1" ends of the backbones and red triangles denote the 2′ ends. The fraction of each structural subclass within the entire ensemble is shown adjacent to the respective averaged backbone conformer models.

Without $MgCl_2$ in 100 mM NaCl, the subclasses identified for PAR_{15} largely displayed similar conformations, with the backbone predominantly bent slightly into an inverted U shape (Fig. 5A).

309 PAR_{22} exhibited similar U-shaped bends, but with additional variations: 21.3% of its
310 conformations were more extended (Fig. 5B, green) and 16.0% more twisted (turquoise), likely
311 contributing to the observed increase in tortuosity (Fig. 4E). Notably, bundles of ADP-ribose units
312 were observed exclusively in PAR_{22} at the 1" ends of each subclass (Fig. 5B), visually confirming
313 our pairwise distance measurements between bases (Fig. S8).

314 The introduction of 1 mM $MgCl_2$ accentuated the conformational differences between PAR_{15} and
315 PAR_{22}. The structural ensembles at 100 mM NaCl of both PARs were generally less connected,
316 exhibiting greater distances between pairs of structures (Fig. S10A-B). However, the presence of
317 Mg^{2+} led to greater similarity among the structures within the ensemble, as evidenced by the
318 increased number of structures demonstrating low root mean square deviations in pairwise
319 comparisons (Fig. S10C-D). Specifically, in PAR_{22}, the occurrence of ADP-ribose bundles was
320 now noted in all five of the identified subclasses, spanning those with extended and more compact
321 conformations (Fig. 5D). This observation is consistent with the heatmap indicating an increase in
322 the number of regions that have short pairwise distance between bases (Fig. S8). The consistent
323 low spatial variance (< 20 Å) in these bundle regions across all subclasses further indicates the
324 systematic presence of bundles throughout the structural ensemble (Fig. 5D). Each bundle
325 contained approximately eight ADP-ribose units at each end, interconnected by six additional
326 units.

327 In contrast, such bundles were not observed in PAR_{15} with 1 mM $MgCl_2$. These conformations
328 closely resembled PAR_{15} in 100 mM NaCl alone, exhibiting similar backbone bending. A small
329 fraction (4.6%) of the structures collapsed into a globule (Fig. 5C, yellow), akin to the most
330 compact conformation observed in our initial MD simulations (Fig. 2). This subclass of collapsed
331 globules may account for the slight 5.3% decrease in R_g in PAR_{15} as observed through SAXS (Fig.
332 3B). These data imply that only a small subset of molecules could undergo relatively featureless
333 collapse with the small amount of Mg^{2+} present, leaving the rest of the ensemble relatively
334 uninfluenced. On the other hand, the widespread bundling of the ADP-ribose units in PAR_{22} could
335 explain the larger 19.0% decrease in its R_g (Fig. 3B).

336

337

338 **PAR Has Less Helicity and Base Stacking Than Poly-adenosine RNA**

339 Our characterization of PAR and its distinct structural features prompted us to draw comparison
340 with poly-adenosine RNA. Though composed of the same ribose, phosphate, and base building
341 blocks, poly-A RNA and PAR have vastly different cellular functions. The former largely acts as
342 a termination signal and binding motif, while the latter functions as a flexible binding scaffold. To
343 delve into structural difference between these two nucleic acids likely tied to their divergent
344 functions, we compared a 15-mer of ADP-ribose (PAR_{15}) to a 30-mer of AMP (rA_{30}) RNA. Both
345 molecules were measured with SAXS in identical solutions containing 100 mM NaCl. Because
346 ADP-ribose (in PAR) contains twice the number of phosphate and ribose groups as AMP (in
347 RNA), these two macromolecules have comparable length and overall charge. Their R_g values
348 further affirmed their similarity (Fig. 6A). Importantly, we chose PAR_{15} for comparison due to its
349 lack of ADP-ribose bundles (Fig. 5), a feature not known to be present in poly-A RNA.

350

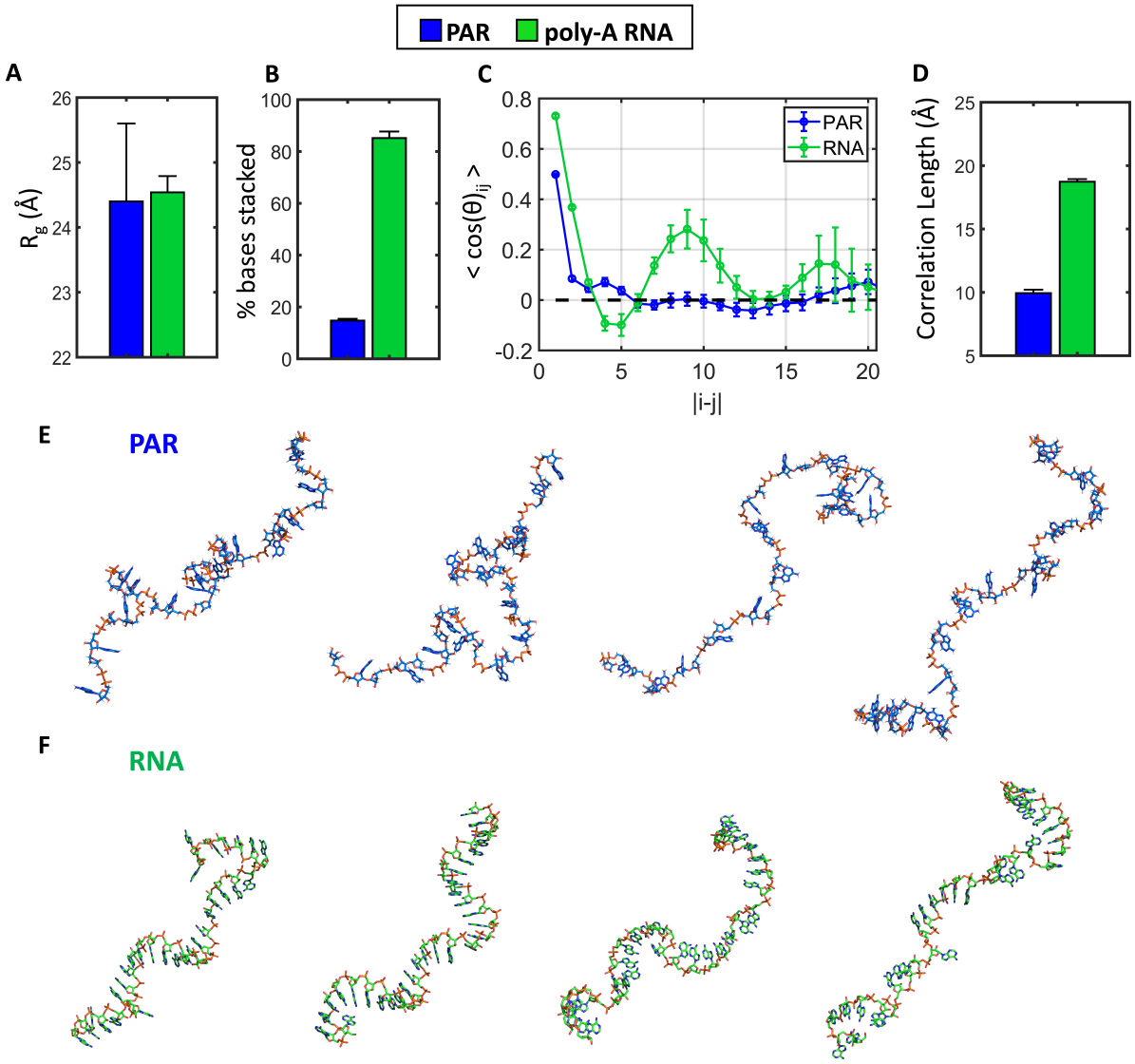

Figure 6. Polymeric differences of PAR_{15} vs poly-adenine RNA (rA_{30}) in 100 mM NaCl. (A) SAXS-derived R_g of PAR_{15} vs rA_{30}. (B) Fraction of adenine bases that are stacked in the PAR_{15} and rA_{30} structural ensembles. (C) Ensemble-averaged orientation correlation functions of PAR_{15}, compared to that of rA_{30}. Error bars represent the variance in the mean. (D) Correlation lengths of PAR_{15} vs rA_{30}, computed across the structural ensembles. (E) Four structures from the conformational ensemble of PAR_{15} that are most highly selected by EOM. (F) Four rA_{30} structures; accessible via SASDFB9 in the Small Angle Scattering Biological Data Bank.[27]

The orientational correlation function (OCF) can describe the orientational alignment of local regions of a polymer chain as a function of distance between its monomers (|i-j|). Peaks in OCF signifies high periodic orientational directionality, while a featureless exponential decay represents

355 random chain orientations.[54] Previous structural characterization of rA_{30} has revealed its well-
356 ordered helix form, attributed to the propensity of adenine bases to undergo π-π interactions. The
357 helix formation is driven by an extensive base stacking network, with 85.2 ± 2.5% of the bases
358 adopting a parallel stacked configuration (Fig. 6B).[48] The OCF of rA_{30} displayed strong oscillatory
359 behavior with peaks spaced by the periodicity of an A-form helix (Fig. 6C). In contrast, PAR_{15}
360 exhibited less orientational correlation along the chain, with the exponential decay of its OCF more
361 closely resembled that of a random coil at $|i-j| > 4$ (Fig. 6C).[54] This difference suggests that the
362 bases in PAR are more randomly arranged than in RNA, supported by the mean PAR correlation
363 length (6.1 ± 0.3 Å) being only a third of that of poly-A RNA (18.7 ± 0.2 Å) (Fig. 6D). The
364 correlation length, which is greater when repeating backbone orientations are present, reflects the
365 lower degree of order for PAR. Moreover, less than 14.4 ± 0.9% of the bases in PAR_{15} were stacked
366 (Fig. 6B), preventing π- π interactions from stabilizing an ordered helical conformation, as
367 observed in rA_{30}. The additional phosphate group and ribose sugar between each adenine base in
368 PAR, compared to poly-A, may place the bases too far apart for extensive π- π base stacking
369 interactions. Such differences in helicity and base stacking were evidently observed in individual
370 sample conformers (Fig. 6E-F).

371

372 **DISCUSSION**

373 Nucleic acid building blocks are reassembled in PAR, a macromolecule that is functionally distinct
374 from RNA. Previously, we have shown that PAR possesses a larger persistence length than RNA,
375 thereby being stiffer, a characteristic attributed to the greater electrostatic repulsion imposed by
376 two phosphates instead of one in RNA per monomer.[23] Both PAR and RNA assume more compact
377 states with increasing salt concentration—a compaction that occurs with 100x fewer divalent than
378 monovalent ions.[23] Building on this polymeric characterization, we set out to explore the 3D
379 structure of PAR. Our studies reveal that the structure of PAR markedly diverges from that of
380 poly-A RNA. In contrast to RNA, PAR possesses a shorter correlation length, exhibits less π-π
381 stacking between bases, and adopts a less helical structure (Fig. 6). These findings are aligned with
382 previous studies showing that PAR, when exposed to only monovalent ions at room temperature,
383 lacks a well-defined secondary structure.[3,47] While the two delocalized rings in adenine make them
384 especially prone to undergo a π-π interaction, the enhanced electrostatic repulsion in PAR relative

385 to RNA could also discourage bases from achieving the close proximity needed to form this
386 interaction. This distinction may align with PAR's unique ability, compared to RNA, to bind
387 positive ligands, both in 1:1 interactions and large-scale condensates.[4,17,18,22]

388 Given that PAR does not form secondary structure and exists as a highly disordered homopolymer,
389 it has historically presented challenges for structural characterization. The few published studies
390 on PAR structure suggested that it lacks a well-defined structure but may have some subtle
391 structural features.[3,47,55] However, a common limitation among these studies is their reliance on
392 data derived from mixtures of PAR lengths, potentially masking signals from individual lengths.
393 In this study, we have synthesized homogenous, single-length PARs for structural investigation.
394 We have integrated structures generated through PAR_{15} and PAR_{22} MD simulations with
395 experimental data offered by SAXS. This approach allows us to determine and analyze plausible
396 heterogeneous ensembles of structures, with a focus on understanding not only how PAR interacts
397 with the ions that surround it but also how its structures are influenced by length.

398 SAXS data revealed that PAR_{22} compacts more than PAR_{15} with Mg^{2+} (Fig. 3). Analysis of order
399 parameters in the SAXS/MD-derived structural ensembles further elucidates differences in Mg-
400 induced PAR compaction between PAR_{15} and PAR_{22}. The additional compaction observed in the
401 latter is driven by a more tortuous backbone (Fig. 4D) and increased stacking among adenine bases
402 (Fig. 4E). These phenomena are mediated by Mg-induced transient contacts with the PAR
403 phosphate backbone, causing local distortion and leading to the more compact configuration
404 observed in the MD trajectories (Fig. S9, Movie S1 and S2).

405 By examining subclasses of the full structural ensembles in real space, we characterized the
406 presence of ADP-ribose bundles unique to PAR_{22} (Fig. 5). This phenomenon aligns with an
407 independent set of MD simulations that observed multiglobular behavior for a 25-mer, based on
408 the dihedral constraints of the molecule.[55] Our approach, combining experimental data with MD
409 simulation, additionally revealed that these ADP-ribose bundles are seeded by the presence of
410 Mg^{2+}, and they are absent in PAR_{15}, enhancing our understanding of the effects of Mg^{2+} on nucleic
411 acids.[56] Once formed, the structural stability of these bundles does not seem to rely on adenine
412 base stacking or direct association with divalent Mg^{2+} ions. Instead, Na^{+} ions within the bundle
413 play a stabilizing role (Movie S2). We speculate that a minimum number of ADP-ribose units are
414 required to form a stable bundle—a critical length not attained by PAR_{15}—possibly due to

insufficient length between bundles to adequately separate congregated negative charges. Ensemble-level pairwise base distance heatmaps support the observation that globular bundles of ADP-ribose units are diffusely present across the entire ensemble in PAR_{22}, but not in PAR_{15} (Fig. S8). It is conceivable that in longer lengths of PAR (>50mer), multiglobular ADP-ribose bundles could periodically appear along the chain, consistent with the beads-on-a-string models of classical polymer theory.[57,58]

These findings lead us to propose a model addressing open questions regarding PAR's various interactions with binding partners that revolves around PAR forming globular ADP-ribose bundles past a critical length that lies between 15 and 22 units. These bundles appear to form through an intra-molecular coil-to-globule phase transition induced by divalent cations, wherein PAR of sufficient length can have part of its chain as a collapsed globule and the rest as an extended polyelectrolyte. Conducting all-atom MD simulations allowed us to characterize this phenomenon whereas observing average system behavior would have missed it. At physiological cationic conditions, we observe that PAR undergoes this transition rapidly on the microsecond timescale. We speculate that these bundles could be of variable size, thereby granting PAR more conformational variety in molecular recognition of binding partners. Additionally, these bundles could serve to localize the negative charge within the molecule, forming super-anion beads-on-a-string (Fig. 7). Follow-up studies are warranted to test these hypotheses.

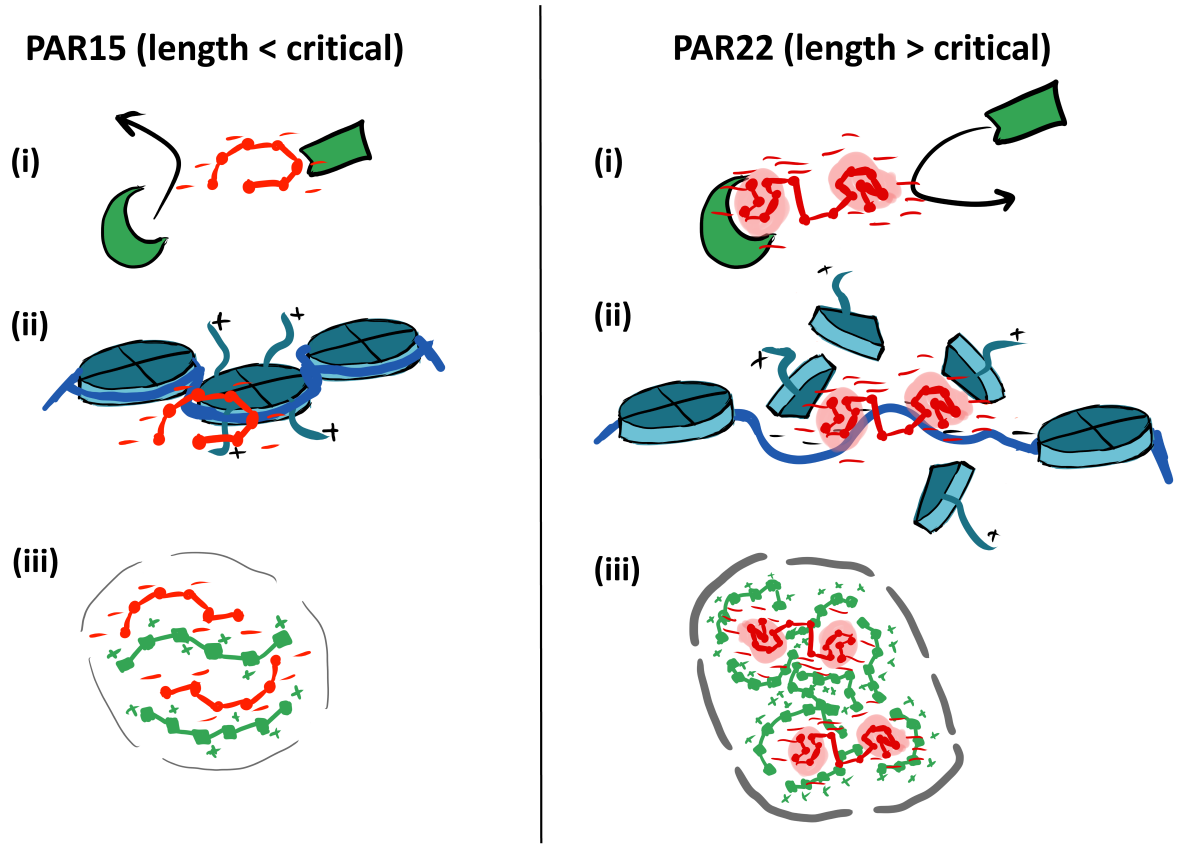

Figure 7. Cartoon model of a possible critical length for coil-to-globule transitions in PAR and potential functional implications. In the presence of 1 mM Mg^{2+}, PAR_{15} is a relatively featureless chain, while PAR_{22} undergoes an intra-chain coil-to-globule transition, forming two ADP-ribose globular bundles. This could work to form distinct conformational motifs in either length of PAR. Collectively, these distinct structural phenotypes may allow one means of (i) molecular specificity in PAR binding to its cognate ligands, where certain PAR readers bind certain PAR motifs. Furthermore, bundling of negative charge through phosphate localization in ADP-ribose clusters is one possible explanation for longer PAR lengths resulting in (ii) histone eviction (observed in Refs 59-61)[59-61] and (iii) enhanced condensate formation (observed in Ref 22).[22] Further studies are warranted to investigate these possible phenomena in more detail.

434

435 **Limitations**

436 In this study, our focus has been on characterizing linear PAR—a choice driven by the current
437 capability in the field to synthesize sufficient, pure quantities of this single defined length
438 molecule, essential for interpretation of SAXS experiments. Consequently, exploring branched
439 PAR, another physiological structural form, is not technically feasible at this juncture. Moreover,

440 synthesizing and simulating specific lengths of long PAR—potentially reaching up to 200-mer in
441 cells—poses notable challenges. Under physiological conditions, PAR is primarily covalently
442 conjugated to proteins, rather than existing as freely diffusing molecules. Given that proteins are
443 conjugated to the ends of PAR, we postulate that ADP-ribose bundles might form in the middle of
444 a chain, possibly exhibiting a periodicity of 15-22 units, rather than exclusively at the ends. Future
445 systematic studies on PAR of different lengths, structures, and conjugations to proteins are
446 essential for a more comprehensive understanding of the structure and function of PAR.

447

448 **Conclusion**

449 In this study we characterized the structure of PAR_{15} and PAR_{22} by performing MD in conjunction
450 with SAXS and carrying out detailed analyses on the resulting conformational ensembles. We
451 showed that PAR rapidly compacts with increasing ionic strength, and that this compaction occurs
452 differently in the two different PAR lengths. The structural ensembles of PAR were found to be
453 highly heterogeneous. By breaking down this heterogeneity through biophysical parameters and
454 real space class averaging, we characterized the conformational mechanism for this difference in
455 compaction, identifying globular bundles of ADP-ribose unique to PAR_{22}. We speculate that this
456 structural feature may enable PAR to bind ligands specifically, forming part of the PAR code.[62]

ACKNOWLEDGEMENTS

We thank Drs. Shirish Chodankar, Richard Gillilan, Qingqiu Huang, and Suzette Pabit for their invaluable support with SAXS data collection. This work is based on research conducted at the Center for High-Energy X-ray Sciences (CHEXS), which is supported by the National Science Foundation (BIO, ENG and MPS Directorates) under award DMR-1829070, and the Macromolecular Diffraction at CHESS (MacCHESS) facility, which is supported by award 1-P30-GM124166-01A1 from the National Institute of General Medical Sciences (NIGMS), National Institutes of Health (NIH), and by New York State's Empire State Development Corporation (NYSTAR). The LiX beamline is part of the Center for BioMolecular Structure (CBMS), which is primarily supported by NIGMS, NIH through a P30 Grant (P30GM133893), and by the DOE Office of Biological and Environmental Research (KP1605010). LiX also received additional support from NIH Grant S10 OD012331. As part of NSLS-II, a national user facility at Brookhaven National Laboratory, work performed at the CBMS is supported in part by the U.S. Department of Energy, Office of Science, Office of Basic Energy Sciences Program under contract number DE-SC0012704. A.A. and K.C. acknowledge support from the NIH via R01-GM137015. The supercomputer time was provided by ACCESS allocation MCA05S028 and Leadership Resource Allocation MCB20012 on Frontera at the Texas Advanced Computing Center. Frontera is made possible by National Science Foundation award OAC-1818253. This work at the Leung lab is supported by the NIH grants T32-CA009110 (M.B.) and R01-GM104135 (A.K.L.L.). Work in the Pollack lab is supported by NIH grant R35-GM122514. T.W. is supported by a Natural Sciences and Engineering Research Council of Canada postgraduate scholarship (NSERC PGS-D).

REFERENCES

1. Dasovich, M. & Leung, A. K. L. PARPS and ADP-ribosylation: Deciphering the complexity with molecular tools. Mol. Cell. **83**(10), 1552-1572 (2023).

2. Lüscher B. *et al.* ADP-ribosyltransferases, an update on function and nomenclature. *The FEBS Journal.* **289**(23, 7399–410 (2022).

3. Schultheisz, H. L., Szymczyna, B. R. & Williamson, J. R. Enzymatic Synthesis and Structural Characterization of 13C, 15N-Poly(ADP-ribose). *J. Am. Chem. Soc.* **131**, 14571–14578 (2009).

4. Gibson, B. A. & Kraus, W. L. New insights into the molecular and cellular functions of poly(ADP-ribose) and PARPs. *Nat. Rev. Mol. Cell Biol.* **13**, 411–424 (2012).

5. Schreiber, V., Dantzer, F., Ame, J.-C. & de Murcia, G. Poly(ADP-ribose): novel functions for an old molecule. *Nat. Rev. Mol. Cell Biol.* **7**, 517–528 (2006).

6. Jin, X., Cao, X., Liu, S. & Liu, B. Functional Roles of Poly(ADP-Ribose) in Stress Granule Formation and Dynamics. *Front. Cell Dev. Biol.* **9**, (2021).

494 7. Leung, A. K. L. *et al.* Poly(ADP-ribose) Regulates Stress Responses and microRNA
495 Activity in the Cytoplasm. *Mol. Cell* **42**, 489–499 (2011).

496 8. Fehr, A. R. *et al.* The impact of PARPs and ADP-ribosylation on inflammation and host–
497 pathogen interactions. *Genes Dev.* **34**, 341–359 (2020).

498 9. Alemasova, E. E. & Lavrik, O. I. A sePARate phase? Poly(ADP-ribose) versus RNA in
499 the organization of biomolecular condensates. *Nucleic Acids Res.* **50**, 10817–10838 (2022).

500 10. Rhine, K., Odeh, H. M., Shorter, J. & Myong, S. Regulation of Biomolecular
501 Condensates by Poly(ADP-ribose). *Chem. Rev.* (2023) doi:10.1021/acs.chemrev.2c00851.

502 11. Alvarez-Gonzalez R, Jacobson MK. Characterization of polymers of adenosine
503 diphosphate ribose generated in vitro and in vivo. *Biochemistry*. **26**(11), 3218–24 (1987).

504 12. Kiehlbauch CC, *et al.* High Resolution Fractionation and Characterization of ADP-
505 Ribose Polymers. *Analytical Biochemistry.* **208**(1), 26–34 (1993).

506 13. Kleczkowska HE, *et al*. Poly ADP-ribosylation in two L5178Y murine lymphoma
507 sublines differentially sensitive to DNA-damaging agents. International Journal of Radiation
508 Biology. **78**(6), 527–34 (2002).

509 14. Malanga M, Althaus FR. Poly(ADP-ribose) molecules formed during DNA repair in
510 vivo. *J Biol Chem*. **269**(26), 17691–6 (1994).

511 15. Teloni, F. & Altmeyer, M. Readers of poly(ADP-ribose): designed to be fit for purpose.
512 *Nucleic Acids Res.* **44**, 993–1006 (2016).

513 16. Reber, J. M. & Mangerich, A. Why structure and chain length matter: on the biological
514 significance underlying the structural heterogeneity of poly(ADP-ribose). *Nucleic Acids Res.* **49**,
515 8432–8448 (2021).

516 17. Löffler, T. *et al.* Influence of chain length and branching on poly(ADP-ribose)–protein
517 interactions. *Nucleic Acids Res.* **51**, 536–552 (2023).

518 18. Dasovich, M. *et al.* Identifying Poly(ADP-ribose)-Binding Proteins with Photoaffinity-
519 Based Proteomics. *J. Am. Chem. Soc.* **143**, 3037–3042 (2021).

520 19. Fahrer, J., Kranaster, R., Altmeyer, M., Marx, A. & Bürkle, A. Quantitative analysis of
521 the binding affinity of poly(ADP-ribose) to specific binding proteins as a function of chain
522 length. *Nucleic Acids Res.* **35**, e143 (2007).

523 20. Kliza *et al*, Reading ADP-ribosylation signaling using chemical biology and interaction
524 proteomics. *Mol. Cell*. **81**, 4552-4567 (2021).

525 21. Fahrer, J. *et al.* High-Affinity Interaction of Poly(ADP-ribose) and the Human DEK
526 Oncoprotein Depends upon Chain Length. *Biochemistry* **49**, 7119–7130 (2010).

527 22. Rhine, K. *et al.* Poly(ADP-ribose) drives condensation of FUS via a transient interaction.
528 *Mol. Cell.* **82**, 969-985.e11 (2022).

529 23. Badiee, M. *et al.* Switch-like compaction of poly(ADP-ribose) upon cation binding. *Proc.*
530 *Natl. Acad. Sci. U. S. A.* **120**, e2215068120 (2023).

531 24. Ando *et al.* ELTA: Enzymatic Labeling of Terminal ADP-Ribose. *Mol. Cell.* **73**, 845-856
532 (2019).

533 25. Slade *et al*. The structure and catalytic mechanism of a poly(ADP-ribose) glycohydrolase.
534 *Nature*. **477**, 616-620 (2011).

535 26. Phillips, J. C. *et al.* Scalable molecular dynamics on CPU and GPU architectures with
536 NAMD. *J. Chem. Phys.* **153**, 044130 (2020).

537 27. J. Huang, S. Rauscher, G. Nawrocki, T. Ran, M. Feig, B. L. de Groot, H. Grubmüller, A.
538 D. MacKerell. CHARMM36m: an improved force field for folded and intrinsically disordered
539 proteins. *Nat. Methods* **14**, 71–73 (2017).

540 28. W. L. Jorgensen, J. Chandrasekhar, J. D. Madura, R. W. Impey, M. L. Klein. Comparison
541 of simple potential functions for simulating liquid water. *J. Chem. Phys.* **79**, 926–935 (1983).

542 29. J. Yoo, A. Aksimentiev. Improved parametrization of Li+ , Na+ , K+ , and Mg2+ ions
543 for all-atom molecular dynamics simulations of nucleic acid systems. *J. Phys. Chem. Lett.* **3**, 45–
544 50 (2012).

545 30. P. F. Batcho, D. A. Case, T. Schlick. Optimized particle-mesh Ewald/multiple-time step
546 integration for molecular dynamics simulations. *J. Chem. Phys.* **115**, 4003–4018 (2001).

547 31. T. A. Darden, D. York, L. Pedersen. Particle mesh ewald: An N log(N) method for ewald
548 sums in large systems. *J. Chem. Phys.* **98**, 10089–92 (1993).

549 32. S. Miyamoto, P. A. Kollman. SETTLE: An analytical version of the SHAKE and
550 RATTLE algorithm for rigid water molecules. *J. Comput. Chem.* **13**, 952–962 (1992).

551 33. H. C. Andersen. RATTLE: A "velocity" version of the SHAKE algorithm for molecular
552 dynamics calculations. *J. Comput. Phys.* **52**, 24–34 (1983).

553 34. Feller, S. E., Zhang, Y., Pastor, R. W. & Brooks, B. R. Constant pressure molecular
554 dynamics simulation: The Langevin piston method. *J. Chem. Phys.* **103**, 4613–4621 (1995).

555 35. Humphrey, W., Dalke, A. & Schulten, K. VMD: Visual molecular dynamics. *J. Mol.*
556 *Graph.* **14**, 33–38 (1996).

557 36. Gowers, R. J. *et al.* MDAnalysis: A Python Package for the Rapid Analysis of Molecular
558 Dynamics Simulations. *Proc. 15th Python Sci. Conf.* 98–105 (2016) doi:10.25080/Majora-
559 629e541a-00e.

560 37. Michaud-Agrawal, N., Denning, E. J., Woolf, T. B. & Beckstein, O. MDAnalysis: a
561 toolkit for the analysis of molecular dynamics simulations. *J. Comput. Chem.* **32**, 2319–2327
562 (2011).

563 38. Yang, L. *et al.* Solution scattering at the Life Science X-ray Scattering (LiX) beamline. *J.*
564 *Synchrotron Radiat.* **27**, 804–812 (2020).

565 39. Acerbo, A. S., Cook, M. J. & Gillilan, R. E. Upgrade of MacCHESS facility for X-ray
566 scattering of biological macromolecules in solution. *J. Synchrotron Radiat.* **22**, 180–186 (2015).

567 40. Hopkins, J. B., Gillilan, R. E. & Skou, S. BioXTAS RAW: improvements to a free open-
568 source program for small-angle X-ray scattering data reduction and analysis. *J. Appl.*
569 *Crystallogr.* **50**, 1545–1553 (2017).

570 41. Skou, S., Gillilan, R. E. & Ando, N. Synchrotron-based small-angle X-ray scattering
571 (SAXS) of proteins in solution. *Nat. Protoc.* **9**, 1727–1739 (2014).

572 42. Riback, J. A. *et al.* Innovative scattering analysis shows that hydrophobic disordered
573 proteins are expanded in water. *Science* **358**, 238–241 (2017).

574 43. Martin, E. W., Hopkins, J. B. & Mittag, T. Chapter Seven - Small-angle X-ray scattering
575 experiments of monodisperse intrinsically disordered protein samples close to the solubility
576 limit. in *Methods in Enzymology* (ed. Keating, C. D.) vol. 646 185–222 (Academic Press, 2021).

577 44. Svergun, D., Barberato, C. & Koch, M. H. J. CRYSOL – a Program to Evaluate X-ray
578 Solution Scattering of Biological Macromolecules from Atomic Coordinates. *J. Appl.*
579 *Crystallogr.* **28**, 768–773 (1995).

580 45. Tria, G., Mertens, H. D. T., Kachala, M. & Svergun, D. I. Advanced ensemble modelling
581 of flexible macromolecules using X-ray solution scattering. *IUCrJ* **2**, 207–217 (2015).

582 46. Bernadó, P., Mylonas, E., Petoukhov, M. V., Blackledge, M. & Svergun, D. I. Structural
583 Characterization of Flexible Proteins Using Small-Angle X-ray Scattering. *J. Am. Chem. Soc.*
584 **129**, 5656–5664 (2007).

585 47. Minaga, T. & Kun, E. Spectral analysis of the conformation of polyadenosine
586 diphosphoribose. Evidence indicating secondary structure. *J. Biol. Chem.* **258**, 725–730 (1983).

587 48. Plumridge, A., Andresen, K. & Pollack, L. Visualizing Disordered Single-Stranded RNA:
588 Connecting Sequence, Structure, and Electrostatics. *J. Am. Chem. Soc.* **142**, 109–119 (2020).

589 49. Chen, H. *et al.* Ionic strength-dependent persistence lengths of single-stranded RNA and
590 DNA. *Proc. Natl. Acad. Sci. U. S. A.* **109**, 799–804 (2012).

591 50. Rambo RP, Tainer JA. Characterizing Flexible and Instrinsically Unstructured Biological
592 Macromolecules by SAS using the Porod-Debye Law. *Biopolymers.* **95**(8), 559–71 (2011).

593 51. Flory PJ. Principles of polymer chemistry. Ithaca, N.Y.: Cornell University Press; 1953.

52. Baul, U., Chakraborty, D., Mugnai, M. L., Straub, J. E. & Thirumalai, D. Sequence Effects on Size, Shape, and Structural Heterogeneity in Intrinsically Disordered Proteins. *J. Phys. Chem. B* **123**, 3462–3474 (2019).

53. Zhao, Z. & Singer, A. Rotationally invariant image representation for viewing direction classification in cryo-EM. *J. Struct. Biol.* **186**, 153–166 (2014).

54. Ullner, M. & Woodward, C. E. Orientational correlation function and persistence lengths of flexible polyelectrolytes. *Macromolecules* **35**, 1437–1445 (2002).

55. D'Annessa, I., Coletta, A. & Desideri, A. Geometrical constraints limiting the poly(ADP-ribose) conformation investigated by molecular dynamics simulation. *Biopolymers* **101**, 78–86 (2014).

56. Pyle, A. M. Metal ions in the structure and function of RNA. *J. Biol. Inorg. Chem. JBIC Publ. Soc. Biol. Inorg. Chem.* **7**, 679–690 (2002).

57. Schoon, T. G. F. Microstructure in solid polymers. *Br. Polym. J.* **2**, 86–91 (1970).

58. Reches, M., Snyder, P. W. & Whitesides, G. M. Folding of electrostatically charged beads-on-a-string as an experimental realization of a theoretical model in polymer science. *Proc. Natl. Acad. Sci. U. S. A.* **106**, 17644–17649 (2009).

59. Poirier, G. G., de Murcia, G., Jongstra-Bilen, J., Niedergang, C. & Mandel, P. Poly(ADP-ribosyl)ation of polynucleosomes causes relaxation of chromatin structure. *Proc. Natl. Acad. Sci. U. S. A.* **79**, 3423–3427 (1982).

60. Panzeter, P. L., Realini, C. A. & Althaus, F. R. Noncovalent interactions of poly(adenosine diphosphate ribose) with histones. *Biochemistry* **31**, 1379–1385 (1992).

61. Realini, C. A. & Althaus, F. R. Histone shuttling by poly(ADP-ribosylation). *J. Biol. Chem.* **267**, 18858–18865 (1992).

62. Leung, A. K. L. Poly(ADP-ribose): A Dynamic Trigger for Biomolecular Condensate Formation. Trends Cell Biol. **30**(5), 370-383 (2020).

For Table of Contents Only
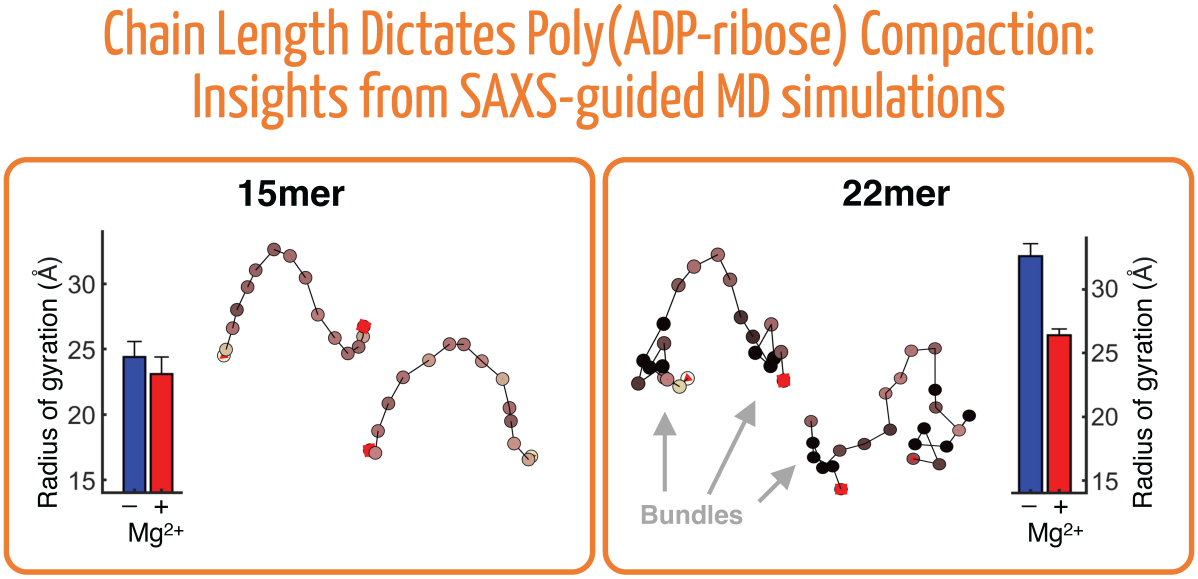
The graphical abstract associated with this submission is provided again here.